Watersheds dynamics following wildfires: Nonlinear feedbacks and implications on hydrologic responses

Fadji Zaouna Maina | Erica R. Siirila-Woodburn

Energy Geosciences Division, Lawrence Berkeley National Laboratory, Berkeley, California

Correspondence Fadji Zaouna Maina, Energy Geosciences Division, Lawrence Berkeley National Laboratory, Berkeley, CA 94720. Email: fadjimaina@lbl.gov

Abstract

In recent years, wildfires in the western United States have occurred with increasing frequency and scale. Climate change scenarios in California predict prolonged periods of droughts with even greater potential for conditions amenable to wildfires. The Sierra Nevada Mountains provide 70% of water resources in California, yet how wildfires will impact watershed-scale hydrology is highly uncertain. In this work, we assess the impacts of wildfires perturbations on watershed hydrodynamics using a physically based integrated hydrologic model in a high-performance-computing framework. A representative Californian watershed, the Cosumnes River, is used to demonstrate how postwildfire conditions impact the water and energy balance. Results from the high-resolution model show counterintuitive feedbacks that occur following a wildfire and allow us to identify the regions most sensitive to wildfires conditions, as well as the hydrologic processes that are most affected. For example, whereas evapotranspiration generally decreases in the postfire simulations, some regions experience an increase due to changes in surface water run-off patterns in and near burn scars. Postfire conditions also yield greater winter snowpack and subsequently greater summer run-off as well as groundwater storage in the postfire simulations. Comparisons between dry and wet water years show that climate is the main factor controlling the timing at which some hydrologic processes occur (such as snow accumulation) whereas postwildfire changes to other metrics (such as streamflow) show seasonally dependent impacts primarily due to the timing of snowmelt, illustrative of the integrative nature of hydrologic processes across the Sierra Nevada-Central Valley interface.

KEYWORDS: climate extremes, integrated hydrologic model, vegetation changes, water management, watershed dynamics, wildfires

1 INTRODUCTION

With the onset of climate change, prolonged periods of droughts and increased temperatures have lead to conditions amenable to forest insect infestation, vegetation mortality, and more frequent and large-scale wildfires (Bowman et al., 2009; Harvey, 2016; McKenzie, Gedalof, Peterson, & Mote, 2004; Westerling, Hidalgo, Cayan, & Swetnam, 2006; Whitlock, 2004). The frequency of wildfires in the western United States has increased by 400% since 1970 with burn areas increasing by 600%, leaving environmental

impacts, which last up to five times longer than historic wildfires (The Nature Conservancy, 2019). In recent years, wildfires in California have doubled in frequency, and the loss of human lives, communities, infrastructure, and subsequent impacts on environmental ecosystems are considerable (Cal Fire, 2019). In November 2018, Northern California was subject to the costliest natural disaster in the world, causing the destruction of more than 60,000 ha of land (Cal Fire, 2019). Projections of California climate predict continued droughts (Cloern et al., 2011; Seager et al., 2007) that have the potential for increases in wildfire frequency and magnitude (McKenzie et al., 2004; Westerling et al., 2006). Seventy percent of water resources in California, the most productive agricultural region in the United States, originate from snowmelt in the Sierra Nevada mountains composed of primarily pines and junipers (Dettinger & Anderson, 2015). However, little is known about how postfire conditions (most notably land cover changes) will impact the dynamics of the hydrologic cycle at large scales. Because vegetation distribution and density are key controls on evapotranspiration (e.g., via canopy interception, root water uptake by plants, and transpiration), it is a crucial modulator of the movement of water and energy from subsurface aquifers to the atmosphere. As such, forest disturbances might seriously affect watershed dynamics as well as the resilience of future water resources.

Previous studies investigating the impact of postwildfire conditions on watershed hydrology were mainly based on experimental studies with a focus on run-off and streamflow (e.g., Benavides-Solorio & MacDonald, 2001; Kunze & Stednick, 2006; Moody & Martin, 2001), evapotranspiration (e.g. Clark, Skowronski, Gallagher, Renninger, & Schäfer, 2012; Nolan, Lane, Benyon, Bradstock, & Mitchell, 2014), soil moisture and infiltration (e.g. Cardenas & Kanarek, 2014; Kinner & Moody, 2010; Robichaud, 2000; Vadilonga, Úbeda, Germann, & Lorca, 2008), and snow dynamics (e.g., Burles & Boon, 2011; Maxwell, Call, & St. Clair, 2019; Musselman, Molotch, & Brooks, 2008). Some modelling studies have been conducted at small scales, with the objective of the analysis of infiltration (Ebel, 2013) or run-off and erosion (Martin, Johnson, Gallaway, & Chaikina, 2011; Rulli & Rosso, 2007). However, large-scale modelling is necessary, and sometimes, the only way to assess the impact of wildfires on watershed hydrology as prefire and postfire measurements are difficult to obtain (Seibert, McDonnell, & Woodsmith, 2010), whereas some studies have modelled larger scales with a focus on the analysis of evapotranspiration (Bond-Lamberty, Peckham, Gower, & Ewers, 2009; Roche, Goulden, & Bales, 2018) and overland flow (Beeson, Martens, & Breshears, 2001; McMichael & Hope, 2007). Large-scale modelling studies are limited in terms of the physics and complexities of the hydrologic mechanisms used to solve above and below ground flow. Examples include the use of the Army Corps of Engineers' Hydrologic Engineering Center Hydrologic Modeling System dendritic routing model (e.g., Cydzik & Hogue, 2009), the conceptual HBV model (Bergström, 1976)

by Seibert et al. (2010), and Fuh's equation (G. Zhou et al., 2015; Wine, Makhnin, & Cadol, 2018). These models fail to assess the intricate interaction of processes occurring across the critical zone interface, which are known to demonstrate strong nonlinearities in important hydrologic processes involved in the water and energy balance near the land surface (Kollet & Maxwell, 2008). Physically based integrated hydrologic models allow for the two-way interaction across the land surface into the vadose and saturated zones of the subsurface (including the connection of the lower atmosphere and vegetation). They are thus an attractive approach to physically understand how postfire perturbations affect snowpack, evapotranspiration, soil moisture and infiltration, run-off, and groundwater storage dynamics.

In this study, we assess the impacts of postfire conditions on watershed-scale hydrodynamics using the physically based integrated hydrologic model ParFlow–Community Land Model (CLM; Kollet & Maxwell, 2006; Maxwell, 2013; Maxwell & Miller, 2005) in a high-performance computing framework. ParFlow simulates water and energy transfer spanning across the earth's critical zone (i.e. from bedrock to vegetation canopy). The CLM (Dai et al., 2003), to which ParFlow is coupled, models land surface processes such as actual evapotranspiration, infiltration, and snow dynamics. Therefore, CLM accounts for spatially distributed vegetation processes including postwildfire land cover changes such as decreases of leaf area index (LAI), reflectance, and albedo. To demonstrate the potential impacts on the integrated hydrologic cycle postwildfire, we study a representative Californian watershed, the Cosumnes Watershed, which spans the Sierra Nevada Mountain and the Central Valley interface. The Cosumnes River hosts one of the last major rivers in California without a dam and is thus a good example of a naturally flowing river without the impacts of large-scale river management. The region is also representative of many Californian watersheds, given that greater than 50% of the watershed's land area resides in the forests of the Sierra Nevada Mountains. Complex hydrological dynamics govern the watershed, including the regional flow of water across an approximately 2,000-m elevation change (from headwaters to sea level), snow accumulation and snowmelt, surface water flow, interflow between surface water, the vadose zone, and groundwater, in addition to irrigation and groundwater pumping primarily in the Central Valley. From a geological point of view, the watershed has formations ranging from low permeability and low storage such volcanic rocks to alluvium materials such as incised valley fill composed of sand and gravels. The watershed, therefore, offers a realistically complex description of an actual system to assess how postwildfire conditions might affect both the individual components of the hydrologic cycle but also the aggregated effect in downstream metrics such as streamflow.

This study quantifies the impact of postwildfire conditions in both time and space on the different processes connecting the atmosphere with the land surface, including changes to evapotranspiration (*ET*), infiltration, snow

water equivalent (*SWE*), and surface water and groundwater storages and pressures. Prewildfire and postwildfire simulations were performed to investigate how these impacts might change depending on the meteorological conditions of the year. We consider two endmember water years: (a) 2015, one of the driest years, and (b) 2017, the wettest year on California record to date. We aim to understand how postwildfire conditions affect watershed-scale hydrologic processes and if some regions are more susceptible to changes in hydrodynamic behaviour following a wildfire than others. Such approaches are useful for science-based decision-making of forest and water management.

2 METHODS

2.1 Study area

The Cosumnes Watershed, approximately 7,000 km^2 in size and is located in Northern California east of Sacramento (Figure 1a), is bounded in the north by the American River and in the south by the Mokelumne River. From a geological point of view, the watershed consists of two predominant zones: Sierra Nevada Mountains, which consist of plutonic rocks, and the Central Valley hosting alluviums such as clays and sands. At the intersection between these two zones, volcanic rocks (basalt and gabbro) incised by consolidated rocks are present. Figure 1b illustrates the strong variation in topography, which includes several steep ridges and valleys adjacent to the main stem of the Cosumnes River. The agricultural region of Central Valley located in the southwest of the watershed consists of different crop types, mainly alfalfa, pasture, and vineyards, and is subject to pumping and irrigation, whereas Sierra Nevada Mountains are covered by predominately evergreen forest (Figure 1c). In the Cosumnes watershed, as in other parts in California, most of the precipitation falls in form of snow in the Sierra Nevada Mountains. As a result, precipitation strongly varies within the watershed; the mountains receive up to 1,500 mm of precipitation per year, whereas rainfall in the Central Valley falls at a rate of approximately 660 mm per year. The yearly average temperature of the Cosumnes Watershed is from 15°C (2.0 version of the North America Land Data Assimilation System data set; Cosgrove et al., 2003). Watershed-average winter temperature can reach 0°C, whereas summers are hot with average temperatures varying between 25°C and 30°C.

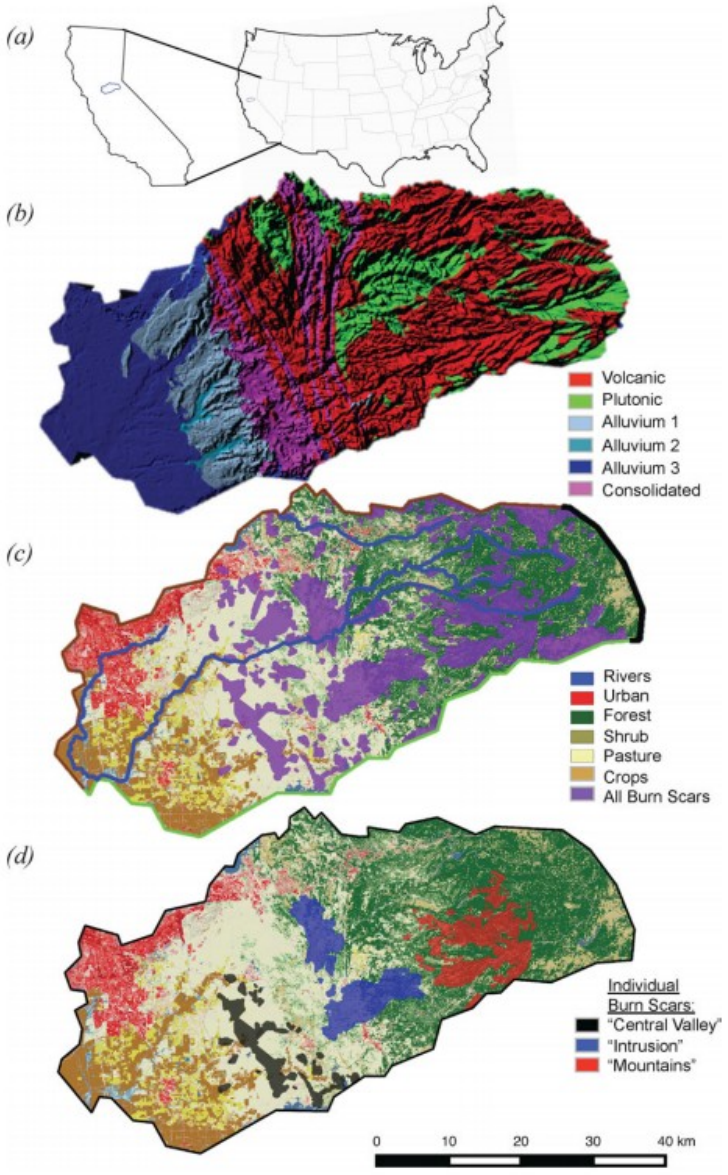

FIGURE 1 (a) Relative location of the Cosumnes watershed. (b) Topography and associated geology of the region where Alluvium 1 represents unconsolidated and semiconsolidated nonmarine deposits, Alluvium 2 represents terrace deposits, and Alluvium 3 represents shale, sandstone, and gravel deposits. (c) Land cover and the historic "burned areas" in the region used in the first sensitivity analysis. Boundary conditions indicated by changes in watershed outline colour. (d) Land cover (see legend in c) and individual burned areas used in postfire mountain 3 scenarios. The following colors correspond to burn areas in each scenario: red, postfire mountains; blue, postfire intrusion; and black, postfire central valley

2.2 Modelling framework

ParFlow-CLM (Kollet & Maxwell, 2006; Maxwell, 2013; R. M. Maxwell & Miller, 2005) simulates three-dimensional flow in the subsurface with Richards equation (Richards, 1931; Equation 1) solved using a finite difference scheme.

$$S_S S_W(\psi_P)\frac{\partial \psi_P}{\partial t} + \varphi \frac{\partial S_W(\psi_P)}{\partial t} = \nabla \cdot [k(x) k_r(\psi_P) \nabla(\psi_P - z)] + q_s, \quad (1)$$

where S_S is the specific storage (L^{-1}), $S_W(\psi_P)$ is the degree of saturation ($-$) associated with the subsurface pressure head ψ_P (L), t is the time, φ is the porosity ($-$), $k(x)$ is the saturated hydraulic conductivity ($L\ T^{-1}$), k_r is the relative permeability ($-$), z is the depth, and q_s is the source/sink term (T^{-1}) including land surface fluxes computed by CLM and pumping.

The Van Genuchten model (van Genuchten, 1980) describes relations between saturation and pressure head and between relative hydraulic conductivity and pressure head. Therefore, the model requires soil characteristics such as hydraulic conductivity, specific storage, porosity, Van Genuchten α, and *n.* Surface flow is calculated with the kinematic wave equation in two dimensions:

$$-k(x)k_r(\psi_0)\nabla(\psi_0 - z) = \frac{\partial\|\psi_0, 0\|}{\partial t} - \nabla.\vec{v}\|\psi_0, 0\| - q_r(x), \quad (2)$$

where $\|\psi_0, 0\|$ indicates the greater term between ψ_0 and 0, $\vec{v}$ is the depth averaged velocity vector of surface run-off ($L\ T^{-1}$), and q_r represents rainfall and evaporative fluxes ($L\ T^{-1}$) computed by CLM.

Ponding depth at the surface in x (υ_x) and y (υ_y) is computed using the following set of equations:

$$\upsilon_x = \frac{\sqrt{S_{f,x}}}{n}\psi_0^{2/3}, \quad (3)$$

$$\upsilon_y = \frac{\sqrt{S_{f,y}}}{n}\psi_0^{2/3}, \quad (4)$$

where $S_{f,x}$ and $S_{f,y}$ friction slopes along x and y, respectively, and n is the manning coefficient.

A terrain following grid is employed in conjunction with a slope derived from a digital elevation model of the watershed topography (Maxwell, 2013). Thus, the stream network is allowed to evolve without preimposed river-network channelling and is shown to reproduce the observed flow channels with high accuracy in the Cosumnes watershed.

Interactions between vegetation, snow, subsurface moisture, and energy fluxes from the lower atmosphere are calculated by a CLM to which ParFlow is coupled (Dai et al., 2003). CLM uses vegetation characteristics (LAI, height, optical properties, stomatal physiology, roughness length, displacement height, etc.; Brunke et al., 2016; Dai et al., 2003; Lawrence et al., 2011) along with eight spatially distributed meteorological variables (precipitation, temperature, east-to-west and north-to-south wind speed, long- and short-wave solar radiation, air pressure, and relative humidity) to force the model at an hourly time step. Water and energy fluxes near the land surface simulated by CLM are informed by the three-dimensional soil moisture distribution as calculated by ParFlow. In this study, vegetation is assumed to be static in CLM, where changes to land cover postwildfire are representative of near-term impacts on the landscape and vegetation regrowth is not considered. As described by Kinoshita and Hogue (2011), whereas vegetation recovery postwildfire is complex, regrowth usually starts after the second year of recovery and is only typically achieved to 90% by the end of the seventh postwildfire year.

2.3 Model development and validation

Numerical models require initial and boundary conditions to solve the nonlinear Richards and kinematic wave equations. We imposed weekly varying values of Dirichlet boundary condition at the American and Mokelumne rivers, whereas a Neumann boundary (i.e., no flow) condition is associated with the eastern part of the watershed (see colour-coded watershed boundaries in Figure 1c). Due to the lack of information on the soil and subsurface hydrodynamic properties within the watershed, as well as their exact spatial distribution, we rely on geological cartography (Jennings, Strand, & Rogers, 1977), literature review, and previous studies (Faunt, 2009; Faunt, Belitz, & Hanson, 2010; Flint, Flint, Thorne, & Boynton, 2013; Gilbert & Maxwell, 2017; Welch & Allen, 2014) to set their values and spatial distributions.

We used the 2011 National Land Cover database (Homer et al., 2015) and maps provided by the National Agricultural Statistics Service of the U.S. Department of Agriculture's Cropland Data Layer (Boryan, Yang, Mueller, & Craig, 2011) to describe land cover and agricultural crop cover. Land and vegetation parameters required by CLM are defined by the International Geosphere-Biosphere Programme (IGBP) database (IGBP, 2018) and further refined to account for specific crop characteristics based on differences in LAI, height, and reflectance. Spatiotemporal variations of the meteorological data are described by the 2.0 version of the North America Land Data Assimilation System forcing database (Cosgrove et al., 2003), which provides hourly atmospheric variables with a resolution of approximately 14 km.

Accurate pumping and irrigation estimates across the Central Valley are difficult to attain given the lack of legal mandates requiring the reporting of subsurface water use in California. We, therefore, estimate values for irrigation rates based on land type and season (the amount of water needed for each type of crop during different parts of the water year). We then derived corresponding pumping rates by assuming that the applied water is sourced from groundwater pumping or river diversions, the latter if a land parcel is adjacent to a river. Fractions of water use between groundwater pumping, and river diversions have been determined using the California Department of Water Resources (California Department of Water Resources, 2010) and the United States Geological Survey (USGS, 2018) databases, which were used in this study to delineate supply proportions. The seasonality of agricultural pumping and irrigation is estimated based on regional climatology and discussions with local stakeholders. For these simulations, we estimate this period to be from April to November.

The developed model has a horizontal resolution of 200 m and is composed of 667 × 400 computational cells per layer. The model's vertical resolution ranges from 10 cm at the land surface to 30 m at the bottom of the domain. The total thickness of the domain is 80 m, discretized over eight layers in the vertical. Simulations utilize high-performance computing to accommodate the large number of cells that constitute the high-resolution model. Land surface processes computed by CLM have been validated using various

remote sensing data sets: Snow Data Assimilation System for SWE (National Operational Hydrologic Remote Sensing Center, 2004), Soil Moisture Active Passive Level 4 for soil moisture (SMAP, 2015), and METRIC for actual *ET* (Allen, Masahiro, & Ricardo, 2007). We also compared simulated groundwater and surface water levels with local measurements. Validation results (see Appendix A) demonstrate a reasonable agreement with simulated results, therefore enabling confidence that the model accurately mimics the complex dynamics of the watershed.

2.4 Simulated scenarios

To assess the postwildfire impacts on watershed hydrology, we consider two cases:

1. A baseline or control case denoted hereafter as the “prefire” scenario, where the watershed is simulated with its prewildfire land cover.
2. A postwildfire case denoted hereafter as the “postfire” scenario, where burn scar areas are represented with barren soil.

As shown in Figure 1c, postfire regions are defined using areal extents of historic burn areas based on past wildfires. Perimeters are defined based on Geographic Information System shapefiles obtained from Cal Fire (Cal Fire, 2019). Although hypothetical burn area perimeters would have been equally as possible in our methodology, in this study, we chose to consider these historic zones because they were once subject to wildfire and are therefore considered vulnerable regions. In this way, studying the impact of historic wildfire burns on system hydrodynamics has the advantages over idealized burn areas in that the former takes into account areas where wildfires are potentially more susceptible to occur. In the postfire simulations, we have replaced any previously defined land use in this prefire case as “barren soil,” again with updated parameterization as defined by the IGBP database. The choice in the barren soil parameterization is in agreement with the postfire land cover described by Pierson and coauthors (Pierson, Robichaud, & Spaeth, 2001) and is meant to be a conservative estimate of potential land cover changes postwildfire.

To account for soil hydrodynamic properties such as hydrophobicity, the presence of ash, and water repellency following a wildfire, we performed additional postfire simulations by assuming that the first layer of the model (i.e., top 10 cm) represents the ash layer, the second layer (between 10 and 40 cm below the land surface) has been burnt, and the deeper layers remain unaffected by the wildfire. Following Ebel and coauthors (2012), we parameterize the ash layer with properties similar to the prefire conditions. The ash layer is known to have good storage properties and a thickness of typically only a few centimeters. The burnt soil layer is parameterized by a decreased hydraulic conductivity value, consistent with many studies (e.g., Ebel & Martin, 2017; Moody, Shakesby, Robichaud, Cannon, & Martin, 2013). Determining the exact degree to which the hydraulic conductivity following a

wildfire is expected to decrease is nontrivial and depends on many parameters such as wildfire severity, recovery period duration, type of soil and land cover, slope and aspect, and so forth. However, many authors suggest that postfire hydraulic conductivity is comprised between 10^{-3} and 10^{-1} m/hr (e.g., D. A. Martin & Moody, 2001; Robichaud, 2000); we, therefore, utilize a value of 10^{-3} m/hr for the burnt soil layer.

Finally, because climate change is also expected to bring more extreme weather events such as increased frequencies and magnitudes of atmospheric rivers (Cloern et al., 2011; Seager et al., 2007), we also perform simulations with different meteorological conditions on the two aforementioned simulation cases. For each of the two test land cover cases, we performed simulations with meteorological forcing based on the following:

- A dry water year: The water year 2015 is one the warmest and driest on California record. The yearly average temperature is approximately 16.2°C, and the yearly average precipitation is 1 mm/day.
- A wet water year: the water year 2017, the wettest year on California record. The average precipitation is approximately 4 mm/day, almost four times greater than the average precipitation in the water year 2015, with the yearly average temperature equal to 2°C less than the water year 2015 average annual temperature.

Three additional postwildfire test cases are used to assess the sensitivity of individual postwildfire conditions in localized areas of the watershed. As shown in Figure 1d, these three test cases correspond to the following:

- *Postfire mountains* (in red): where the wildfire occurs in the upper part of the watershed corresponding to the Sierra Nevada Mountains;
- *Postfire intrusion* (in blue): where the wildfire occurs in the intermediate area of the watershed (i.e., in the intrusion of volcanic rocks);
- *Postfire central valley* (in black): where the wildfire occurs in the Central Valley.

3 RESULTS AND DISCUSSIONS

In this section, land surface and subsurface processes are compared for the prewildfire and postwildfire cases in both time and space. Land surface processes include *ET*, infiltration, and *SWE.* Subsurface dynamics are measured by the variation of surface water and groundwater storages and pressure heads (indicating the groundwater levels or hydraulic heads). For each of these output metrics, we computed the relative difference quantified by the following unitless metric:

$$\Delta X_{i,t} = \frac{X_{pre-fire_{i,t}} - X_{post-fire_{i,t}}}{X_{pre-fire_{i,t}}}, \quad (5)$$

where X is the model output (ET, infiltration, SWE, or pressure head ψ) at a given point i and time t.

3.1 Soil property changes

Preliminary simulations to determine the relative impacts of land cover alone and land cover combined with changes to soil properties following a wildfire indicate that land cover is the main parameter controlling the hydrodynamics at the watershed scale. As discussed in the subsequent sections below, land cover changes in the Sierra Nevada forests have a high impact on snow dynamics in the upper watershed, which is also consistent with several other studies (e.g., Broxton et al., 2015; Harpold et al., 2014; Maxwell et al., 2019; Musselman et al., 2008; Varhola, Coops, Weiler, & Moore, 2010), which subsequently impact down-gradient flow regimes in the watershed. Additionally, because most of the historic wildfires occurred in regions overlying lower hydraulic conductivity subsurface properties (volcanic rocks with a hydraulic conductivity inferior to 10^{-6} m/hr) and because we assume ash layer has no effect on these nonmacroporous soils, the impact of changing the burn scar soil properties in the models was found to be minimal (differences were less than 0.1% for total groundwater storage and 2% for the total surface water storage). Based on these simulation results, as well as the great uncertainties related to postfire hydraulic conductivity values and their evolution in time, we focus only on the land cover changes in the following results.

3.2 Evapotranspiration (ET)

ET, the largest component of surface energy balance, is a combination of evaporation from the ground, canopy surfaces, and sublimation and transpiration by plants. CLM computes evapotranspiration flux based on the available soil moisture and evaporative demand specific to vegetation type as specified in each cell. Figure 2 shows the comparison of total daily ET within the watershed obtained with the postfire and prefire simulations for the (a) dry and (b) wet water year. As expected by a decrease in forest cover, total daily ET is lower in the postfire when compared to the prefire simulation. Decreases of ET following wildfire have been documented in many studies (Bond-Lamberty, Peckham, Gower, & Ewers, 2009; Clark et al., 2012; Nolan et al., 2014; Roche, Goulden, & Bales, 2018, and references therein). This trend is also consistent regardless of wet or dry year (Figure 2a vs. Figure 2b). However, we recall that the model does not take into account vegetation dynamics and thus factors such as vegetation grow-back density are not considered, which may make ET potentially higher following a wet year. The annual domain-averaged difference between the prefire and postfire ET ($\Delta ET_{i,t}$) calculated with the use of Equation 5 is equal to $7.7\ 10^{-2}$ for the wet year and $9.23\ 10^{-2}$ for the dry year. Despite the annual domain averages, the wet and dry year$\Delta ET_{i,t}$ being similar, the fluctuations in ET trends throughout the water year are quite different (see Figure 2).

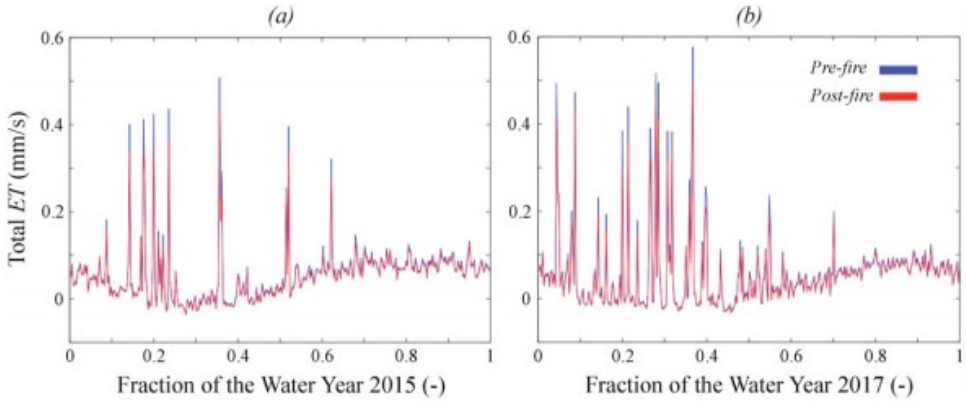

FIGURE 2 Comparison of total daily *ET* within the watershed obtained with postfire (red lines) and prefire (blue lines) for the (a) dry and (b) wet water years

For the two water years, Figure 3 depicts the spatial distribution of $\Delta ET_{i,t}$ at two selected times (a single snapshot in the winter, at a fraction of the water year equal to 0.3, and in the summer, at a fraction of the water year equal to 0.9) for the two water years. $\Delta ET_{i,t}$ is nonzero only in the burn scar areas; other areas (indicated by the shadow) show a $\Delta ET_{i,t}$ equal to or nearly equal to zero. As shown in the colour bar, white areas correspond to burn areas with little change in *ET* postfire, red areas denote burn areas with *ET* lower than the prefire, and blue areas denote burn areas with *ET* higher than the prefire. Surprisingly, Figure 3 shows that many regions exhibit greater postfire *ET* compared to the prefire conditions (blue regions representing around 10% of the total burn area). Because of the counterintuitive nature of these trends, these areas are of specific interest. Spatially, these regions appear down-gradient of larger burn areas in the mountains, where an increase in flow results in greater levels of ponded water at the surface, and thus higher evaporation potential. This result illustrates how first-order assumptions in postfire conditions are not always valid, depending on the complex nature of the hydrologic system. Other watershed-scale spatial trends are also evident in Figure 3. Regardless of season or year, areas located in the Central Valley are less sensitive to postwildfire land cover changes (with $\Delta ET_{i,t}$ inferior to 0.5) compared to areas located in the Sierra Nevada mountains ($\Delta ET_{i,t}$ close to 1.0). Whereas trends related to snowpack dynamics may be responsible for the lack of sensitivity in the lower elevation, the geologic composition of the subsurface is also another likely factor.

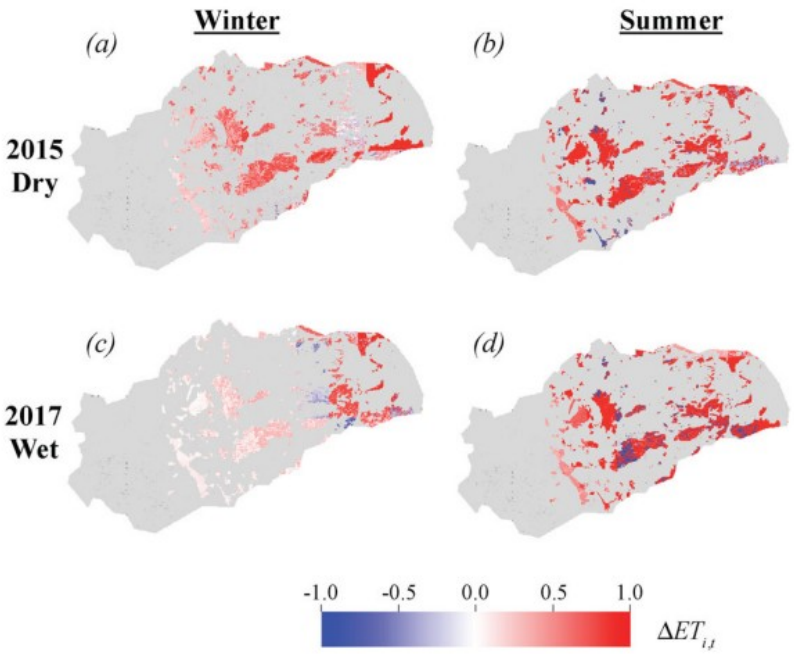

FIGURE 3 Spatial distributions of $\Delta ET_{i,t}$ at two selected times: winter (a and c) and summer (b and d). The top row shows the differences in the dry water year (2015), and the bottom row shows differences in the wet water year (2017). Grey regions show nonburn areas. As shown in the colour bar, white areas correspond to burn areas with little change in *ET* postfire, red areas denote burn areas with *ET* lower than the prefire, and blue areas denote burn areas with *ET* higher than the prefire

Table 1 lists the annual average of $\Delta ET_{i,t}$ for each type of geological formation. Only areas residing in the burn scar regions are considered in the average. Volcanic, plutonic, and consolidated rocks have the highest variation, on the order of 8 to 10 times greater than the variations in the alluvium aquifers. Among bedrock formations, volcanic rocks are the most sensitive to postwildfire conditions, where postwildfire *ET* rates dramatically decrease compared to the prewildfire condition. This is due to the hydrodynamic properties of these rocks, which are characterized by low permeability and storage parameters. Changes in *ET* are therefore linked to the geology that controls the water quantity and availability and thus the amount of water that can be used by plants. In the absence of vegetation (i.e., zero transpiration), soil evaporation is the main component of *ET*, which will depend on the quantity of water available in the soil but also on the ability of the soil to allow the water to evaporate. In the case of volcanic rocks characterized by very low permeability and storage, the soil is water limited, as such *ET* decreases. This is why the high permeability and storage areas (such as Central Valley alluvial aquifers) are less sensitive to changes in land cover postfire. The more permeable the rock, the less susceptible an area to the changes in *ET* following a wildfire.

TABLE 1 Annual average of $\Delta ET_{i,t}$ for each type of geological formation

Water year	Consolidated rock	Alluvium 1	Alluvium 2	Alluvium 3	Plutonic	Volcanic
Dry	18.7	2.82	2.23	2.07	16.4	20.6
Wet	16.8	0.5	3.18	2.21	22.0	25.7

3.3 Infiltration

As vegetation changes impact *ET* fluxes and therefore energy balance at the land surface, they could also affect infiltration representing the quantity of water from the atmosphere entering the subsurface. Infiltration is indeed calculated in the model based on the soil characteristics along with soil moisture and available water at the land surface, which in turn depends on the energy balance. Figure 4 shows the comparison of total daily infiltration obtained with the postfire and prefire simulations for the two water years. Differences between the two cases are minimal. A close inspection of the results reveals that the total daily infiltration decreases in the postfire simulations.

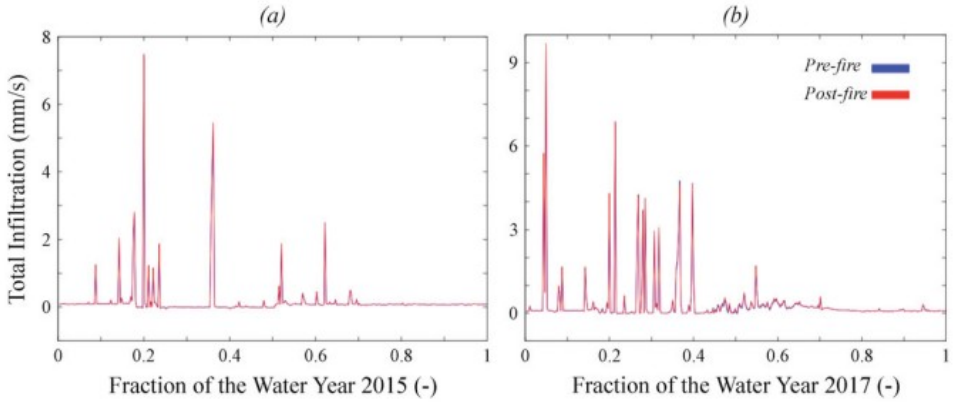

FIGURE 4 Comparison of total daily infiltration within the watershed obtained with the postfire (red lines) and prefire (blue lines) simulations for the (a) dry 2015 water year and (b) wet 2017 water years

Table 2 shows annual averages of $\Delta Infiltration_{i,t}$ for the different geologic units. As indicated by the positive $\Delta Infiltration_{i,t}$ values in Table 2, the decrease in infiltration after a wildfire is consistent with previous studies (Cardenas & Kanarek, 2014; Kinner & Moody, 2010; Robichaud, 2000). In our case, this decrease in infiltration is due to an increase in subsurface saturation and subsequent increases in Dunne (i.e., saturation excess) flow, which results in greater movement of water via run-off as opposed to infiltration. Indeed, in the absence of vegetation, and therefore zero canopy interception and lower *ET*, the amount of water reaching the ground surface is higher, which causes a greater propensity of rapid soil saturation. Our results show that the decrease in infiltration is higher in rocks with lower storage and permeability such as volcanic, plutonic, and consolidated rocks (see Table 2). Due to their hydrodynamic (i.e., water retention) properties, these rocks store less water, and therefore, even a small amount of water reaching the ground is sufficient to cause soil layer saturation and inhibit infiltration.

TABLE 2 Annual average of $\Delta Infiltration_{i,t}$ for each type of geological formation

Water year	Consolidated rock	Alluvium 1	Alluvium 2	Alluvium 3	Plutonic	Volcanic
Dry	0.00122	9.8910^{-5}	0.0047	0.00026	0.061	0.0028
Wet	3.610^{-5}	5.0110^{-6}	0.00259	$6.22\ 10^{-5}$	0.02	0.022

3.4 Snow water equivalent

The evolution of snowpack accumulation and snowmelt is quantified through SWE, the amount of water contained within the snowpack in units of water depth. Figure 5 shows the total *SWE* for the (a) dry and the (b) wet water years. The postfire simulations (red lines) show an increase in the accumulated *SWE* when compared to the prefire simulations (blue lines). The differences between *SWE* obtained with postfire and the prefire are rather marked in the middle of winter when peak *SWE* occurs. Because vegetation is likely to control only the degree to which *SWE* accumulates, it is logical that the difference between the prefire and postfire simulations are predominantly in terms of the magnitude of the snowpack in Figure 5, not the timing (which depends on the meteorological forcing). The degree to which vegetation contributes to ablation, however, could affect the timing of snowpack dynamics. However, from our results, we show that this effect is minimal, as the prefire and postfire curves are predominately offset in magnitude, not in time.

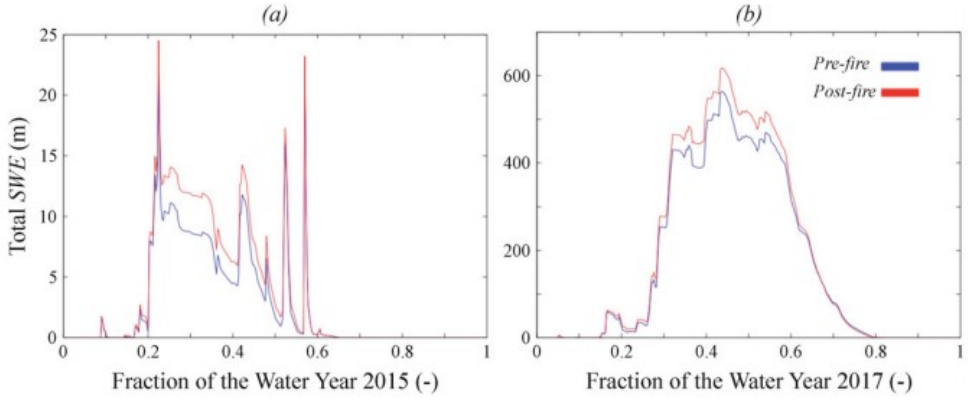

FIGURE 5 Comparison of total *SWE* within the watershed obtained with postfire (red lines) and prefire (blue lines) simulations for the (a) dry 2015 and (b) wet 2017 water years. Note the different scale of the *y* axes depending on the water year

In the absence of vegetation, and thus canopy interception, the majority of precipitation falling as snow will reach the ground and accumulate, hence the high amount of *SWE* observed in the postfire simulation. It should be noted that changes to albedo (i.e., a dark bare surface vs. a forest canopy) will impact the energy balance at the land surface and thus a nonlinear relationship between snowfall and accumulation in the absence of vegetation could be expected. Our results are in agreement with other studies (Burles & Boon, 2011; Gleason, Nolin, & Roth, 2013; Winkler, Boon, Zimonick, & Spittlehouse, 2014) that report an increase of 10% to 60% *SWE* after a wildfire.

Figure 6 shows the spatial distribution of $\Delta SWE_{i,t}$ at a selected time during the winter (water year fraction equal to 0.3). Only results from the wet year are shown here (1) because the spatial distributions of snow-covered areas are similar for the two simulated years, and (2) the values of $\Delta SWE_{i,t}$ are very

low for the dry year. Thus, we focus on the wet year characterized by significant $\Delta SWE_{i,t}$ to correctly perform comparisons. Similar to the trends observed for *ET* (Figure 3), only the areas within the burn scar perimeters are associated with non-zero $\Delta SWE_{i,t}$ (see Figure 6a). Although we only see increases in *SWE* in the postwildfire simulations (denoted by blue areas), the magnitude of $\Delta SWE_{i,t}$ is not the same for all these areas. By superimposing the spatial distribution of $\Delta SWE_{i,t}$ over the topography of the upper-elevation watershed (Figure 6b), we notice that postwildfire burn areas located in topographic depressions that have the greatest $\Delta SWE_{i,t}$. On barren soils, *SWE* accumulation appears to be higher in areas of intermediate topographic relief. It is well known from snowpack surveys that snowpack accumulation in the context of wildfires is topographically complex (Ellis, Pomeroy, Essery, & Link, 2011; Maxwell et al., 2019). Our findings illustrate that apart from the climatic conditions and the land surface type, slope and aspect control the variations of *SWE* in postwildfire environments, which is consistent with previous studies. The impact of orography on snow accumulation and snowmelt in postwildfire forests is driven primarily through the amount of radiation reaching the land surface. Under forest cover, differences in shortwave radiation due to slope and aspect are minimal. However, in the absence of forest cover topographic self-shading of north-facing slopes can contribute to substantial differences in shortwave irradiance between opposing open south-facing and north-facing hillslopes. As vegetation changes, the effect of shortwave radiation (which depends on the slope and aspect) becomes more pronounced, leading to a nonuniform change of *SWE.*

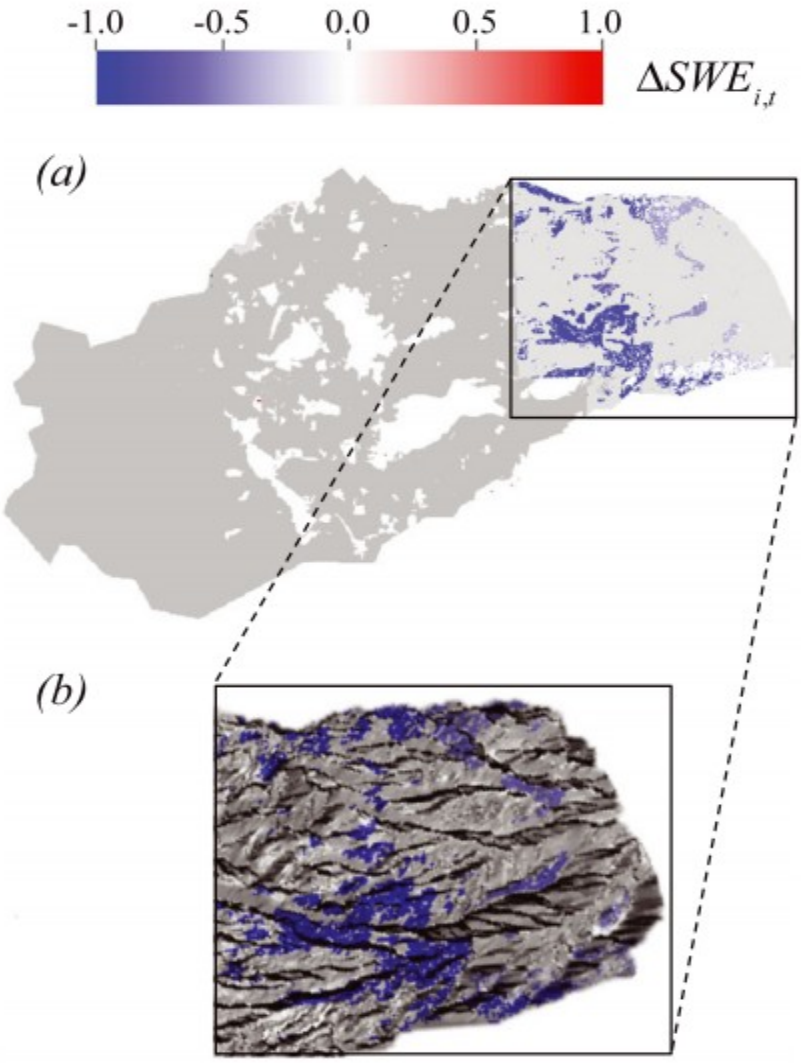

FIGURE 6 (a) Spatial distribution of $\Delta SWE_{i,t}$ at a selected time (water year fraction equal to 0.3) in the winter of the wet 2017 water year. As in Figure 3, grey areas denote nonburn areas. White areas correspond to burn areas with little change from the prefire, and blue areas correspond to burn areas with *SWE* is higher than the prefire. Our results indicate that there are not any burn areas where postfire *SWE* is lower than the prefire. In (b), we superimposed an elevation relief map over the upper elevation region of the model domain to highlight correlations between changes in postfire *SWE* and topography

3.5 Surface and groundwater flow

ET, infiltration, and *SWE* dynamics ultimately impact surface and subsurface storage, yet the nature of their watershed-scale connectivity is highly uncertain. In this section, we study how postfire conditions affect the surface

water and the groundwater, with direct implications for water supply in the Central Valley. We do so by analysing (1) the spatial distributions of surface and groundwater levels indicated by the distribution of simulated pressure head at the land surface and (2) groundwater and surface water budgets.

Surface water storage $Storage_{SW}$ (L^3) is calculated by

$$Storage_{SW} = \sum_{i=1}^{n_{SW}} \Delta x_i \times \Delta y_i \times \psi_i, \quad (6)$$

where n_{SW} is the total number of river cells (L); Δx_i and Δy_i are cell discretizations along the x and y directions (L), respectively; and i indicates the cell. Note that because ParFlow-CLM is an integrated hydrologic model, only surface cells whose pressure is greater than 0 are taken into account in the surface water storage summation.

Groundwater storage $Storage_{GW}$ (L^3) is calculated by

$$Storage_{GW} = \sum_{i=1}^{n_{GW}} \Delta x_i \times \Delta y_i \times \Delta z_i \times \psi_i \times (S_{si}/\phi_i), \quad (7)$$

where n_{GW} is the total number of subsurface saturated cells (−) and Δz_i is the discretization along the vertical direction the cell (L).

3.5.1 Surface water

As documented in many studies, wildfires and vegetation disturbances directly affect the surface water dynamics by increasing run-off. This component of the hydrologic cycle is widely studied in the context of wildfires and land cover changes (e.g., Benavides-Solorio & MacDonald, 2001; Kunze & Stednick, 2006; Moody & Martin, 2001; Moody, Shakesby, Robichaud, Cannon, & Martin, 2013; Siirila-Woodburn, Steefel, Williams, & Birkholzer, 2018; Y. Zhou, Zhang, Vaze, Lane, & Xu, 2013). Figure 7 shows a comparison of the total surface water storage obtained with the prefire and postfire simulations for the two studied years. As expected, in the postfire simulation, surface water storage is higher than in the prefire simulation, but interestingly, we notice that this increase in surface water storage is only substantial beginning in the spring for dry year (water year fraction approximately 0.4) and in the summer for the wet year (water year fraction approximately 0.6). During the fall and winter seasons at the beginning of the simulation, surface water storage is nearly equivalent in the postfire and prefire simulations. Recall from Figure 5 that postfire conditions lead to a higher amount of accumulated snow and therefore more water moving down gradient in the watershed later in the water year. It is important to note that because the majority of wildfires generally occur in the upper region of the watershed, the balance of snowpack timing is even more impacted given the majority of precipitation in these higher elevation regions falls in the form of snow instead of rain. In winter, precipitation contributes to snowpack instead of immediate (or nearly immediate) surface water run-off and increased streamflow. Additionally, the lack of vegetation in the postfire simulation changes the surface roughness (i.e., bare soil is less rough than forest

cover), and as such, the surface flow becomes more rapid once snowmelt occurs.

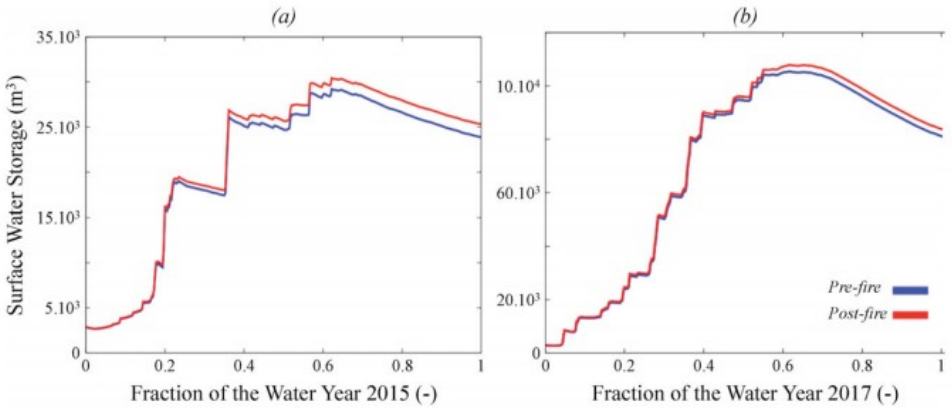

FIGURE 7 Comparison of total surface water storage within the watershed obtained with postfire (red lines) and prefire (blue lines) for the (a) dry and (b) wet water years

Figure 8 shows an analysis of the spatial distribution of the relative difference of pressure differences between the prefire and postfire simulations at the land surface $\Delta\psi_{i,t}$. Two selected times are shown (during the winter, at a fraction of water year 0.3, and during the summer, at a fraction of water year 0.9) for the 2 years. Unlike the spatial results for *ET* and *SWE*, changes in postwildfire pressure distributions are not limited to the spatial extent of historic wildfire burn areas. Dispersed changes (both positively and negatively relative to the prefire) are present throughout the watershed. Figure 8 shows that the spatial distributions of pressure differ according to the season, where the propagation of pressure distribution changes due to the postwildfire conditions are more dispersed in the summer season (Figures 8a and 8c). In winter, the $\Delta\psi_{i,t}$ are more marked in postwildfire burn areas. These areas are generally the same for the dry and wet year. Surface pressure generally increases in the postwildfire simulations (blue regions in Figure 8). This can be attributed to the lack of canopy interception in the postfire conditions, which leads to a higher amount of water from precipitation reaching the land surface, and more water ponding compared to the prefire environment. In general, increases in surface pressure are higher in the Sierra Nevada Mountains due to the hydrodynamic properties of the subsurface. This finding supports the conclusions previously stated regarding the local increase in *ET* due to the surface saturation. The decreases in infiltration postwildfire are also in agreement with the pressure results shown here, as rapid saturation in the low-permeability regions will result in precipitation contributing to increased run-off.

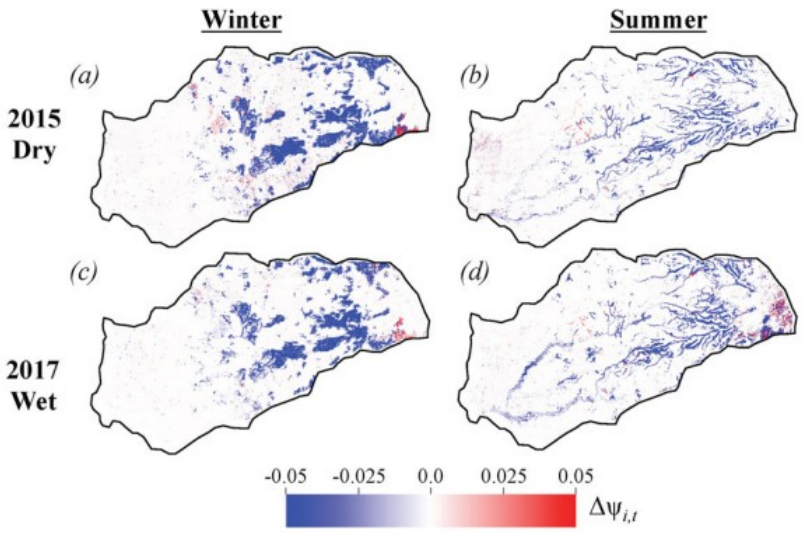

FIGURE 8 Spatial distributions of surface $\Delta\psi_{i,t}$ at two selected times: winter (a and c) and summer (b and d). The top row (a and b) shows the differences between prefire and postfire conditions in the dry 2015 water year, and the bottom row (c and d) shows differences in the wet 2017 water year

During the summer, postwildfire conditions show an impact throughout most of the watershed area and are not limited to regions solely within the burn-scar areas. This is evident predominantly in surface water generating areas (such as the main branch of the Cosumnes and other larger tributaries). Recall that differences between the prefire and postfire simulations for the total surface water storage are low during the winter, whereas in the summer the changes in postwildfire surface water storage are most apparent, especially for the wet year (Figure 8d). Indeed, during the wet year, the amount of accumulated snow is high, and therefore, the snowmelt fed the streamflow during the spring and summer. Thus, we see the most dramatic and nonlinear differences between the prewildfire and postwildfire simulations during the summer of the wet year (Figure 8d).

We highlight that although wildfires were primarily simulated over bedrock areas, in the summer of the wet year, the $\Delta\psi_{i,t}$ in the Central Valley are actually higher than in the bedrock regions of the Sierra Nevada Mountains. This is due to the hydrodynamic properties of these two zones. In the Sierra Nevada Mountains, the surface roughness (as parameterized by the manning coefficient) is lower than that of the Central Valley, and therefore, the surface flow is faster. As such, snowmelt from higher elevations will quickly flow through the Sierra Nevada Mountains and reach the Central Valley where the flow is slower (again, due to the manning coefficient, but also because elevation grades are lower), which causes a large increase in surface storage in the area. We also notice that the so-called “area of influence” of the pressure distribution becomes much wider along with stream segments in the Central Valley, as flow accumulates through the lower reaches of the Cosumnes and its associated tributaries.

As mentioned in Section 1, by simulating a complex system with an integrated physically based model, our study aims to provide realistic insights into when and where run-off will increase following a wildfire. We

computed the maximum differences in pressure $Max(\Delta_e\psi)_i$ between prewildfire and postwildfire simulations for each cell along the Cosumnes River and its tributaries using the following equation:

$$Max(\Delta_e\psi)_i = \max\left(\left(\psi_{post-fire} - \psi_{pre-fire}\right)_{i,1:ndt}\right), \quad (8)$$

where *ndt* is the total number of time steps for each year equal to 8,760.

Maximum changes in water level in the Cosumnes River and tributaries following a wildfire are shown in Figure 9. Our results indicate that in the postfire conditions, the water level in the Cosumnes River and tributaries can rise up to 3 m at a given time. This increase in streamflow is more pronounced in the wet water year where most of the areas show an increase greater than 2 m, whereas the for dry water year 2015, the high increase in streamflow is mostly observed down-gradient in the Central Valley and along the portion of the Cosumnes River located in the upper part corresponding to the Sierra Mountains.

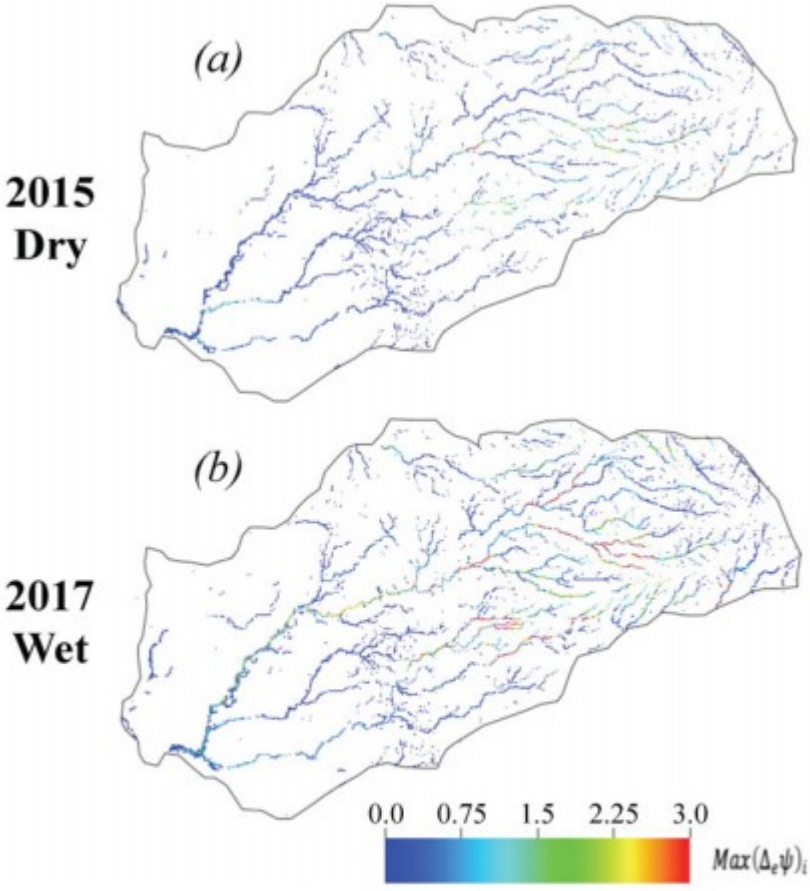

FIGURE 9 Spatial distributions of the maximum change in water level (in m) in the river in the postfire conditions for (a) the dry 2015 and (b) the wet 2017 water years

3.5.2 Groundwater

Figure 10 depicts the total groundwater storage within the watershed obtained with the postfire and prefire simulations for the (a) dry and (b) wet water years. Contrary to surface water storage, groundwater storages obtained with the two test cases are quite similar. It should be noted, however, that the relative volumes of water are quite different, where groundwater storage is several orders of magnitude larger. We also note that a slight increase in groundwater storage does exist in the postfire simulation during the summer. To determine where this increase in subsurface pressure occurs, Figure 11 shows the spatial distributions of $\Delta\psi_{i,t}$ at the bottom layer of the subsurface model for a snapshot in time during the summer season (water year fraction equal to 0.9) for the 2 years of interest. In general, postwildfire subsurface pressure is greater than the prefire (blue areas). Some interspersed areas of the opposite (red areas) are apparent in the upper part of the watershed and appear to be uncorrelated with any parameterization of the model. For the dry year (Figure 11a), the pressure differences are highest in the Sierra Nevada Mountains and the incision of consolidated rocks within the volcanic intrusion. These subsurface $\Delta\psi_{i,t}$ are nonzero mainly over burn scar areas, where the impacts of groundwater-surface water interactions are greatest. For the wet year (Figure 11b), these same areas show sensitivity to postfire conditions. Furthermore, fluvial regions in closer proximity to the rivers also show greater pressure variation following the wildfire. The subsurface pressure differences between the prefire and postfire simulations are due to the combined effects of

- a generally lower ET and lack of canopy interception in the postwildfire simulation, in which near surface subsurface pressure gradients will generally move water downward toward the groundwater instead of upward back in the atmosphere;
- the physical properties of the rocks, where low higher permeability regions show greater pressure increases associated with the degree of vertical flow in those geologic units; and
- the exchange between surface water and groundwater, as surface water storage increases due to seasonal snowmelt, the rivers and tributaries fill and become flashier. The former explains the increase in pressure in the areas near the rivers. In the Sierra Nevada Mountains, these exchanges are most often localized in zones with relatively high permeability. In the Central Valley, these exchanges are more diffuse and take place more consistently along the Cosumnes River and its tributaries.

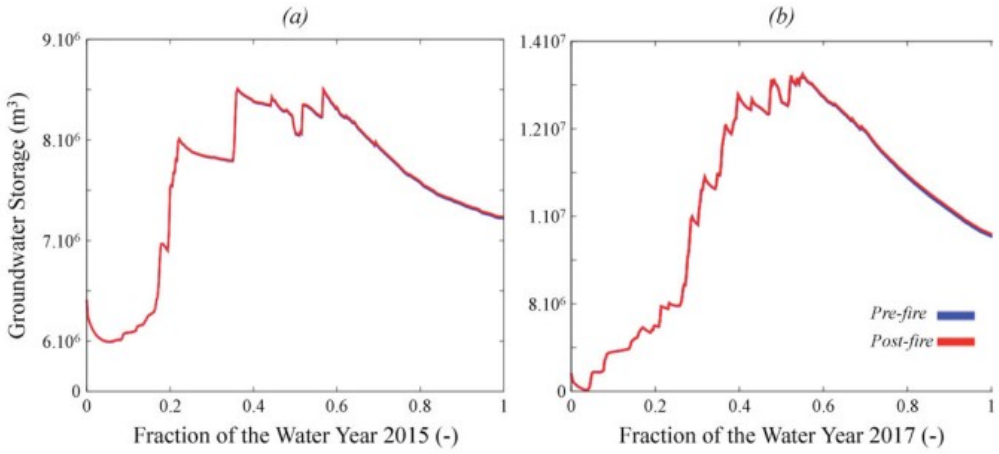

FIGURE 10 Comparison of total groundwater storage within the watershed obtained with postfire (red lines) and prefire (blue lines) simulations for the (a) dry 2015 and (b) wet 2017 water years

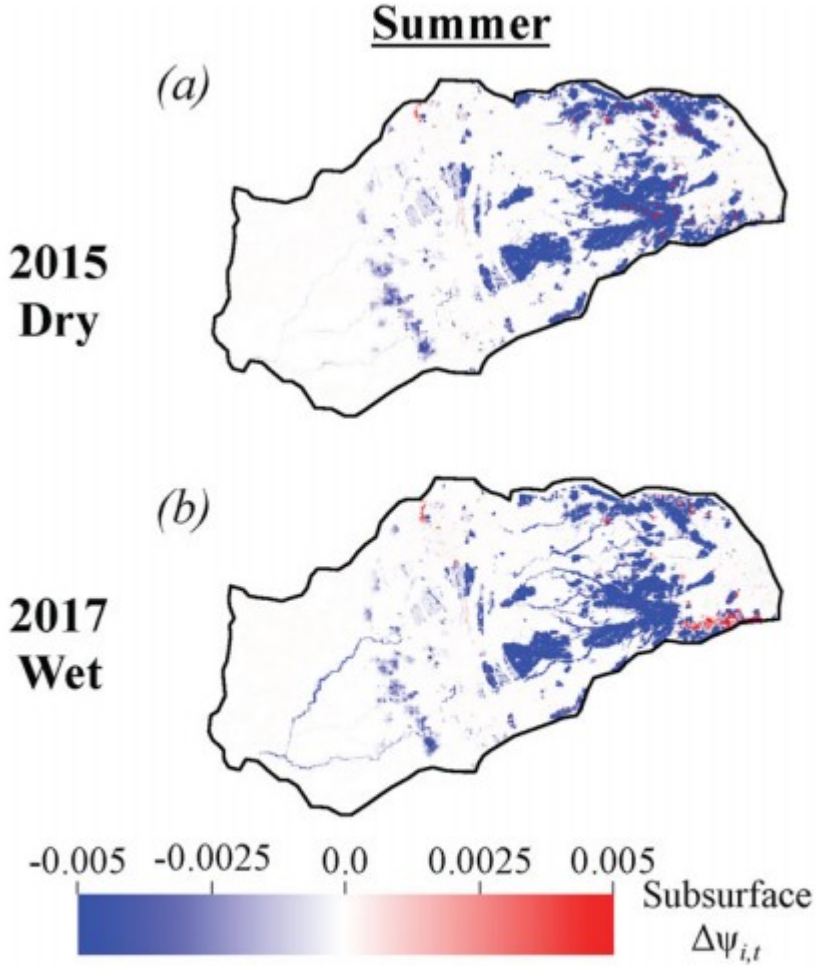

FIGURE 11 Summer spatial distributions of subsurface $\Delta\psi_{i,t}$ for the (a) dry 2015 water year and the (b) wet 2017 water year. Subsurface $\Delta\psi_{i,t}$ for the winter season are not shown

Lastly, we note that although the vegetation has not been removed everywhere in the intrusion, groundwater pressure changes in this zone are substantial. This is due to the geological setting of the area (see Figure 1a) that consists of highly nonpermeable volcanic rocks incised with consolidated rocks, which are characterized by a higher permeability and storage. Due to the structure of the area, small changes in surface pressure or atmosphere-subsurface connectivity will mainly affect the incision of consolidated rocks.

3.6 Sensitivity of postfire locations

In the previous section, we simulated postfire conditions based on historic wildfire burn extents spanning and all the three zones of the watershed (Sierra Nevada Mountain Range, Central Valley, and Intrusion) as a proof of concept. These simulations are meant to demonstrate the compounded effects of realistic changes to land cover in the aftermath of a wildfire, and a

“worst-case” scenario. This approach allowed us to better understand the change in hydrodynamics that may occur as a function of the rock type and relative position within the watershed with regard to proximity to rivers, other land use types, topography, and so forth. In this section, we investigate how localized postfire changes might affect the adjoining hydrology of the watershed. For the sake of brevity in discussing these test case results, we show the simulation results for only the wet year (2017). We focus on the temporal variations of the model outputs because the spatial distributions of postwildfire dynamics have already been discussed in the previous sections.

Using the individual burn scar spatial extents defined in Figure 12 shows the impact of postfire conditions on the following metrics: (a) *ET*, (b) *SWE*, (c) surface water storage, and (d) groundwater storage. In general, the impacts of burn scars in the Central Valley are minimal, indicating that postwildfire changes to vegetation occurring in the Central Valley are much less likely to cause a change in large-scale watershed hydrodynamics. In contrast, wildfires occurring in the upper part of the watershed (*postfire mountains*) have a greater impact. This is due to the feedbacks and controls of water distribution in this system, which, like most of California's watersheds, has feedbacks that are controlled by the Sierra Nevada Mountains hydrodynamics that propagate downward to lower elevations.

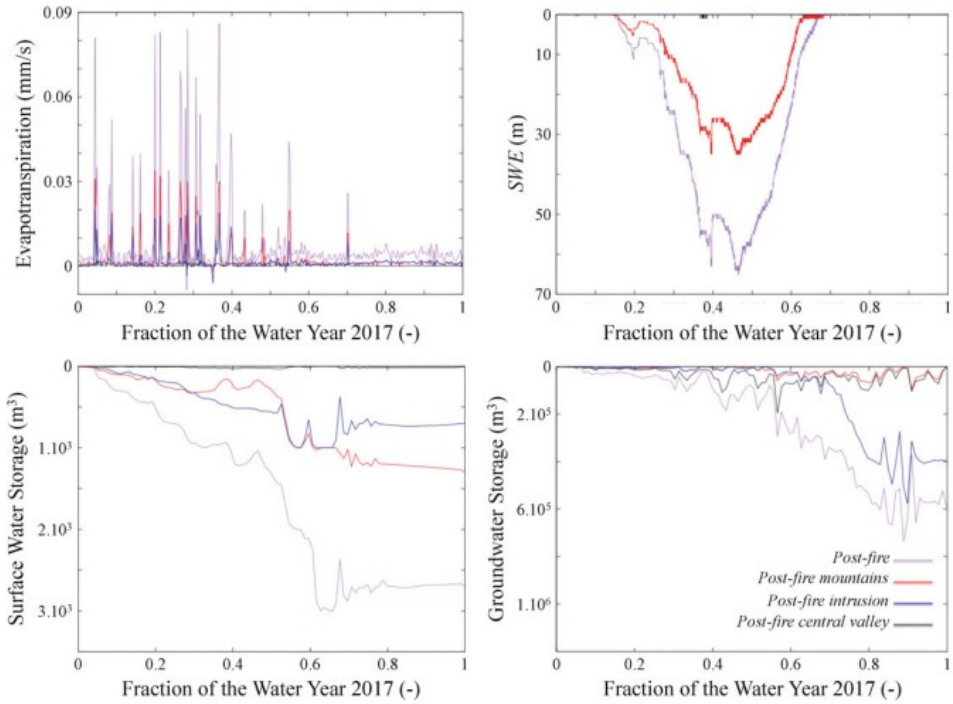

FIGURE 12 Differences between prefire and the three cases for the wet 2017 water year for total: (a) *ET*, (b) *SWE*, (c) surface water storage, and (d) groundwater storage within the watershed

An analysis of the temporal variability of *ET* (Figure 12a) indicates that postfire mountains have the highest *ET* approaching that of the postfire. *ET*

trends obtained with the *postfire central valley* are identical to the prefire, whereas *postfire intrusion ET* trends are slightly greater than the prefire. Results for *SWE* (Figure 12b) show unsurprisingly that only postfire mountains (in addition to postfire as discussed previously) lead to an increase in *SWE.* As a consequence, the middle- to late-season (water year fraction greater than 0.6) surface water flow as well as the increase in groundwater storage in the summer of postfire mountains is greater than in the other cases. We notice however that even if the *SWE* in postfire intrusion is identical to the prefire, the surface water storage of postfire intrusion (Figure 12c) is slightly higher than the prefire surface water storage, indicating that the wildfires perturbations alone in the Sierra Nevada Mountains without a *SWE* accumulation induce an increase in surface storage and therefore groundwater storage (Figure 12d) due to the exchange. This is due to the change of the surface roughness, which causes an increase in run-off. We further remark that between fractions of water year 0.4 and 0.5, the increase of surface water storage in postfire intrusion is greater than in postfire mountains. This period corresponds to the winter snowpack accumulation (as shown in Figure 12b). In postfire intrusion, there is no increase in *SWE* relative to the prefire; therefore, all the nonintercepted precipitation will contribute to run-off, whereas in postfire mountains, precipitation increases *SWE* and contributes to a greater summer run-off. An analysis of the variation of groundwater storage (see Figure 12d) highlights that the groundwater storage increases more in postfire intrusion than in postfire mountains despite the large increase of surface water storage in postfire mountains. This is due to the location of the wildfire in postfire intrusion, which is close to the Central Valley where run-off will likely increase the groundwater storage more rapidly.

We did not observe a significant change in the watershed hydrology in the postfire central valley simulation due to its geological properties, land cover, topography, and location (downstream of the watershed). As discussed above, the changes in watershed-scale hydrology following postwildfire perturbations are due to the increase in *ET*, run-off, and *SWE* and decrease in infiltration. These variations occur more predominantly in areas characterized by steep and complex slopes and low permeability, which is not the case of the Central Valley. These test cases demonstrate that depending on the area where the wildfire occurs, the impacts on the watershed hydrology may differ, and wildfires occurring in the higher elevations in this type of geologic setting have the highest impact on subsequent flow and storage.

4 CONCLUSIONS

In this study, we investigated the impacts of postwildfires land and soil property changes on watershed-scale hydrology. An integrated hydrologic model of a representative Californian watershed, the Cosumnes, was used to demonstrate the nonlinear feedbacks. Our results show that postwildfire land cover changes lead to the following:

- Predominantly a decrease in evapotranspiration (*ET*), which depends on the type of rock over which the wildfire occurs. Our results suggest that the most sensitive formations to postwildfire changes in *ET* are the rocks characterized by low permeability and storage capacity. Increases in *ET* were also observed in some regions down-gradient of burn scars where the amount of water available for *ET* increases in postfire environments. This illustrates the complex counterintuitive trends between postfire conditions, surface water generation, and interactions with vegetation.
- An increase in snow accumulation in a nonuniform way within the watershed. Results show that the degree of snow accumulation due to postwildfire conditions depends predominately on topography. Areas located in the depressions and lower elevations were found to be the most sensitive.
- Run-off changes, most significantly in summer when the seasonal snowmelt is occurring. Whereas postwildfire changes in run-off are mainly due to the altered snowpack dynamics, decreases in surface roughness due to postwildfire perturbations also impact the flashiness of streamflow, with more impacts observed in the Central Valley than in the mountains. Our results also highlight that postwildfire increase in surface water flow causes an increase in groundwater storage due to the exchange between surface water and groundwater.

The timing of postwildfire impacts on *ET*, *SWE*, and infiltration is most driven by the individual climate of wet or dry water years, where prewildfire and postwildfire conditions of these metrics vary more in terms of magnitude, not timing. Postwildfire impacts on streamflow, however, revealed a delayed impact due to the increased magnitudes of snowpack accumulated earlier in the water year. Postfire perturbations are likely to increase soil moisture and water storages in the summer, mainly by retaining more snow at the land surface and reducing canopy interception, and *ET.* Lastly, our results show that in a typical Californian watershed such as the one simulated here, the connected nature of postwildfire perturbations occurring in the Sierra Nevada Mountains will likely have a greater impact on watershed hydrology the one occurring in the Central Valley.

This analysis has allowed us to better understand how postwildfire conditions will affect watershed hydrology in California, a region where wildfires are becoming more frequent, large in scale, and more devastating. These simulations highlighted sometimes counterintuitive feedbacks that occur following a wildfire and provide a framework for us to identify the regions most sensitive to wildfires, as well as the hydrologic processes that are most affected. The validation procedure has certainly shown that the integrated hydrologic model is able to reproduce both measured and satellite-based data; however, the results presented in this work are embedded with uncertainties inherent in any numerical modelling originating from the lack

of data and the assumptions in the representation of the physics considered here.

Although it was outside of the scope of this analysis, future studies should take into account the vegetation dynamics during the year. As shown in this study, the increase in water storage occurring in the postfire conditions will likely to contribute to vegetation growth. Additionally, depending on the year (wet or dry), vegetation growth might change, leading to a change of dynamics. Sensitivity analyses could be conducted in future studies to assess the impact in conjunction with fire severity mapping and as a function of lag time since the wildfire. Lastly, although in this work, we relied on historic fire perimeters to assess how postwildfire affects the nonlinear hydrodynamics occurring at watershed scale, this work also has implications on other human and/or environmental disturbances, which may be subject to similar landscape changes as the ones simulated here.

ACKNOWLEDGMENTS

This work was supported by https://doi.org/10.13039/100007000 (LDRD) funding from Berkeley Lab, provided by the Director, Office of Science, of the U.S. Department of Energy under Contract DE-AC02-05CH11231. This research used computing resources from the National Energy Research Scientific Computing Center, a DOE Office of Science User Facility supported by the http://dx.doi.org/10.13039/100006132 of the U.S. Department of Energy under Contract No. DE-AC02-05CH11231.

DATA AVAILABILITY STATEMENT

The data that support the findings of this study are available from the corresponding author upon request.

APPENDIX A:

COMPARISONS BETWEEN MODEL OUTPUTS AND SATELLITE-BASED PRODUCTS AND MEASUREMENTS

To validate the model, we performed a simulation over a period of 5 years (from the water year 2013 to the water year 2017) with an hourly time step. To define the initial conditions in terms of pressure head, we interpolated groundwater level measurements of 16 piezometers by kriging. We then used the result of the kriging to carry out a steady state simulation with an average of precipitation minus evapotranspiration as forcing. The results of these steady state simulations were then used as initial conditions for the 5-year period simulations. Because these initial conditions are an approximation, we considered the first 2 years as a period of relaxation and performed model validation only for the water years 2015–2017. We compared the simulated land surface processes with the data obtained from remote sensing techniques, and the simulated pressure-head in the aquifer and the rivers with measurements. However, we would like to note that the watershed has very few measurements, only one piezometer has continuous

hydraulic heads measurements every 2 weeks, and for several years, also only one station measures water level in the Cosumnes River at an hourly time step since the 1990s.

Our comparisons suggest that the model is in reasonable agreement with the METRIC data set for the total evapotranspiration fluxes, SNODAS and Parallel Energy Balance (ParBal) method for the SWE and SMAP for soil moisture (Figure A1). Simulated pressure head in the groundwater and the Cosumnes River are also fairly consistent with measurements with an average error inferior to 0.5 m (Figure A2). The differences between measured and simulated river heights are certainly due to a gauge threshold or water management effects.

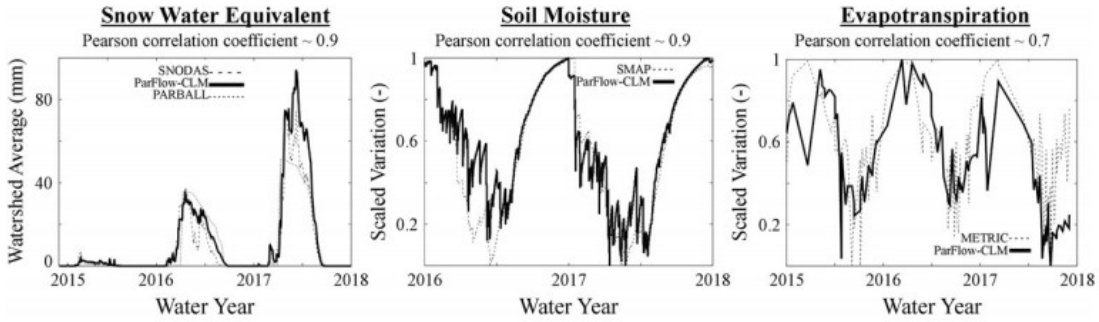

FIGURE A1 Comparisons between simulated land surface processes (snow water equivalent, evapotranspiration, and infiltration) and satellite-based products. CLM, Community Land Model; SMAP, Soil Moisture Active Passive; SNODAS, Snow Data Assimilation System

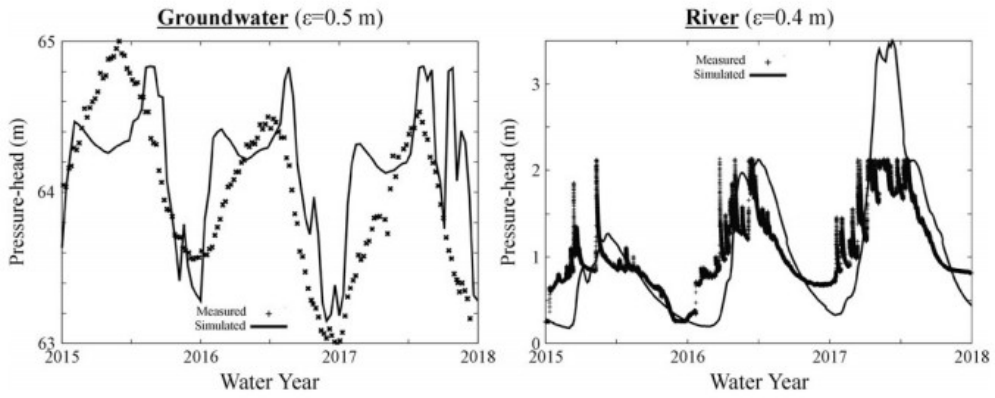

FIGURE A2 Comparisons between simulated and measured groundwater and surface water levels

REFERENCES

Allen, R. G., Masahiro, T., & Ricardo, T. (2007). Satellite-Based Energy Balance for Mapping Evapotranspiration with Internalized Calibration (METRIC)—Model. *Journal of Irrigation and Drainage Engineering*, 133(4), 380– 394. https://doi.org/10.1061/(ASCE)0733-9437(2007)133:4(380)

Beeson, P. C., Martens, S. N., & Breshears, D. D. (2001). Simulating overland flow following wildfire: mapping vulnerability to landscape disturbance. *Hydrological Processes*, 15(15), 2917– 2930. https://doi.org/10.1002/hyp.382

Benavides-Solorio, J., & MacDonald, L. H. (2001). Post-fire runoff and erosion from simulated rainfall on small plots, Colorado Front Range. *Hydrological Processes*, 15(15), 2931– 2952. https://doi.org/10.1002/hyp.383

Bergström, S. (1976). *Development and application of a conceptual runoff model for Scandinavian catchments. Department of Water Resources Engineering*. Lund Institute of Technology: University of Lund.

Bond-Lamberty, B., Peckham, S. D., Gower, S. T., & Ewers, B. E. (2009). Effects of fire on regional evapotranspiration in the central Canadian boreal forest. *Global Change Biology*, 15(5), 1242– 1254. https://doi.org/10.1111/j.1365-2486.2008.01776.x

Boryan, C., Yang, Z., Mueller, R., & Craig, M. (2011). Monitoring US agriculture: The US Department of Agriculture, National Agricultural Statistics Service, Cropland Data Layer Program. *Geocarto International*, 26(5), 341–358. https://doi.org/10.1080/10106049.2011.562309

Bowman, D. M. J. S., Balch, J. K., Artaxo, P., Bond, W. J., Carlson, J. M., Cochrane, M. A., … Pyne, S. J. (2009). Fire in the Earth system. *Science*, 324(5926), 481– 484. https://doi.org/10.1126/science.1163886

Broxton, P. D., Harpold, A. A., Biederman, J. A., Troch, P. A., Molotch, N. P., & Brooks, P. D. (2015). Quantifying the effects of vegetation structure on snow accumulation and ablation in mixed-conifer forests. *Ecohydrology*, 8(6), 1073– 1094. https://doi.org/10.1002/eco.1565

Brunke, M. A., Broxton, P., Pelletier, J., Gochis, D., Hazenberg, P., Lawrence, D. M., … Zeng, X. (2016). Implementing and evaluating variable soil thickness in the Community Land Model, Version 4.5 (CLM4.5). *Journal of Climate*, 29(9), 3441– 3461. https://doi.org/10.1175/JCLI-D-15-0307.1

Burles, K., & Boon, S. (2011). Snowmelt energy balance in a burned forest plot, Crowsnest Pass, Alberta, Canada. *Hydrological Processes*, 25(19), 3012– 3029. https://doi.org/10.1002/hyp.8067

Cal Fire. (2019). Cal Fire. Retrieved January 28, 2019, from http://fire.ca.gov/

California Department of Water Resources. (2010). California Department of Water Resources. Retrieved October 18, 2018, from https://water.ca.gov/

Cardenas, M. B., & Kanarek, M. R. (2014). Soil moisture variation and dynamics across a wildfire burn boundary in a loblolly pine (Pinus taeda) forest. *Journal of Hydrology*, 519, 490– 502. https://doi.org/10.1016/j.jhydrol.2014.07.016

Clark, K. L., Skowronski, N., Gallagher, M., Renninger, H., & Schäfer, K. (2012). Effects of invasive insects and fire on forest energy exchange and evapotranspiration in the New Jersey pinelands. *Agricultural and Forest*

Meteorology, 166–167, 50– 61. https://doi.org/10.1016/j.agrformet.2012.07.007

Cloern, J. E., Knowles, N., Brown, L. R., Cayan, D., Dettinger, M. D., Morgan, T. L., … Jassby, A. D. (2011). Projected evolution of California's San Francisco Bay-Delta-River System in a century of climate change. *PLOS ONE*, 6(9), e24465. https://doi.org/10.1371/journal.pone.0024465

Cosgrove, B. A., Lohmann, D., Mitchell, K. E., Houser, P. R., Wood, E. F., Schaake, J. C., … Meng, J. (2003). Real-time and retrospective forcing in the North American Land Data Assimilation System (NLDAS) project. *Journal of Geophysical Research: Atmospheres*, 108(D22). https://doi.org/10.1029/2002JD003118

Cydzik, K., & Hogue, T. S. (2009). Modeling postfire response and recovery using the Hydrologic Engineering Center Hydrologic Modeling System (HEC-HMS)1. *JAWRA Journal of the American Water Resources Association*, 45(3), 702– 714. https://doi.org/10.1111/j.1752-1688.2009.00317.x

Dai, Y., Zeng, X., Dickinson, R. E., Baker, I., Bonan, G. B., Bosilovich, M. G., … Yang, Z.-L. (2003). The Common Land Model. *Bulletin of the American Meteorological Society*, 84(8), 1013– 1024. https://doi.org/10.1175/BAMS-84-8-1013

Dettinger, M., & Anderson, M. L. (2015). Storage in California's reservoirs and snowpack in this time of drought. *San Francisco Estuary and Watershed Science*, 13(2). https://doi.org/10.15447/sfews.2015v13iss2art1

Ebel, B. A. (2013). Simulated unsaturated flow processes after wildfire and interactions with slope aspect. *Water Resources Research*, 49(12), 8090–8107. https://doi.org/10.1002/2013WR014129

Ebel, B. A., & Martin, D. A. (2017). Meta-analysis of field-saturated hydraulic conductivity recovery following wildland fire: Applications for hydrologic model parameterization and resilience assessment. *Hydrological Processes*, 31(21), 3682– 3696. https://doi.org/10.1002/hyp.11288

Ellis, C. R., Pomeroy, J. W., Essery, R. L. H., & Link, T. E. (2011). Effects of needleleaf forest cover on radiation and snowmelt dynamics in the Canadian Rocky Mountains. *Canadian Journal of Forest Research*, 41(3), 608– 620. https://doi.org/10.1139/X10-227

Faunt, C. C., Belitz, K., & Hanson, R. T. (2010). Development of a three-dimensional model of sedimentary texture in valley-fill deposits of Central Valley, California, USA. *Hydrogeology Journal*, 18(3), 625– 649. https://doi.org/10.1007/s10040-009-0539-7

C. C. Faunt, & Geological Survey (U.S.) (Eds.) (2009). *Groundwater availability of the Central Valley Aquifer, California*. Reston, Va: U.S. Geological Survey.

Flint, L. E., Flint, A. L., Thorne, J. H., & Boynton, R. (2013). Fine-scale hydrologic modeling for regional landscape applications: The California Basin Characterization Model development and performance. *Ecological Processes*, 2(1), 25. https://doi.org/10.1186/2192-1709-2-25

Gilbert, J. M., & Maxwell, R. M. (2017). Examining regional groundwater–surface water dynamics using an integrated hydrologic model of the San Joaquin River basin. *Hydrology and Earth System Sciences*, 21(2), 923– 947. https://doi.org/10.5194/hess-21-923-2017

Gleason, K. E., Nolin, A. W., & Roth, T. R. (2013). Charred forests increase snowmelt: Effects of burned woody debris and incoming solar radiation on snow ablation. *Geophysical Research Letters*, 40(17), 4654– 4661. https://doi.org/10.1002/grl.50896

Harpold, A. A., Biederman, J. A., Condon, K., Merino, M., Korgaonkar, Y., Nan, T., … Brooks, P. D. (2014). Changes in snow accumulation and ablation following the Las Conchas Forest Fire, New Mexico, USA. *Ecohydrology*, 7(2), 440– 452. https://doi.org/10.1002/eco.1363

Harvey, B. J. (2016). Human-caused climate change is now a key driver of forest fire activity in the western United States. *Proceedings of the National Academy of Sciences*, 113(42), 11649– 11650. https://doi.org/10.1073/pnas.1612926113

Homer, C., Dewitz, J., Yang, L., Jin, S., Danielson, P., Xian, G., … Megown, K. (2015). Completion of the 2011 National Land Cover Database for the conterminous United States—Representing a decade of land cover change information. *Photogrammetric Engineering & Remote Sensing*, 81(5), 345–354.

IGBP. (2018). Global plant database published - IGBP [Text]. Retrieved October 18, 2018, from http://www.igbp.net/news/news/news/globalplantdatabasepublished.5.1b8ae20512db692f2a6800014762.html

Jennings, C. W., Strand, R. G., & Rogers, T. H. (1977). *Geologic map of California*. Sacramento, Calif.: Division of Mines and Geology.

Kinner, D. A., & Moody, J. A. (2010). Spatial variability of steady-state infiltration into a two-layer soil system on burned hillslopes. *Journal of Hydrology*, 381(3), 322– 332. https://doi.org/10.1016/j.jhydrol.2009.12.004

Kollet, S. J., & Maxwell, R. M. (2006). Integrated surface–groundwater flow modeling: A free-surface overland flow boundary condition in a parallel groundwater flow model. *Advances in Water Resources*, 29(7), 945– 958. https://doi.org/10.1016/j.advwatres.2005.08.006

Kollet, S. J., & Maxwell, R. M. (2008). Capturing the influence of groundwater dynamics on land surface processes using an integrated, distributed watershed model. *Water Resources Research*, 44(2). https://doi.org/10.1029/2007WR006004

Kunze, M. D., & Stednick, J. D. (2006). Streamflow and suspended sediment yield following the 2000 Bobcat fire, Colorado. *Hydrological Processes*, 20(8), 1661– 1681. https://doi.org/10.1002/hyp.5954

Lawrence, D. M., Oleson, K. W., Flanner, M. G., Thornton, P. E., Swenson, S. C., Lawrence, P. J., … Slater, A. G. (2011). Parameterization improvements and functional and structural advances in Version 4 of the Community Land Model. *Journal of Advances in Modeling Earth Systems*, 3(1). https://doi.org/10.1029/2011MS00045

Martin, D. A., & Moody, J. A. (2001). Comparison of soil infiltration rates in burned and unburned mountainous watersheds. *Hydrological Processes*, 15(15), 2893– 2903. https://doi.org/10.1002/hyp.380

Martin, Y. E., Johnson, E. A., Gallaway, J. M., & Chaikina, O. (2011). Negligible soil erosion in a burned mountain watershed, Canadian Rockies: Field and modelling investigations considering the role of duff. *Earth Surface Processes and Landforms*, 36(15), 2097– 2113. https://doi.org/10.1002/esp.2236

Maxwell, J. D., Call, A., & St. Clair, S. B. (2019). Wildfire and topography impacts on snow accumulation and retention in montane forests. *Forest Ecology and Management*, 432, 256– 263. https://doi.org/10.1016/j.foreco.2018.09.021

Maxwell, R. M. (2013). A terrain-following grid transform and preconditioner for parallel, large-scale, integrated hydrologic modeling. *Advances in Water Resources*, 53, 109– 117. https://doi.org/10.1016/j.advwatres.2012.10.001

Maxwell, R. M., & Miller, N. L. (2005). Development of a Coupled Land Surface and Groundwater Model. *Journal of Hydrometeorology*, 6(3), 233– 247. https://doi.org/10.1175/JHM422.1

McKenzie, D., Gedalof, Z., Peterson, D. L., & Mote, P. (2004). Climatic change, wildfire, and conservation. *Conservation Biology*, 18(4), 890– 902. https://doi.org/10.1111/j.1523-1739.2004.00492.x

McMichael, C. E., & Hope, A. S. (2007). Predicting streamflow response to fire-induced landcover change: Implications of parameter uncertainty in the MIKE SHE model. *Journal of Environmental Management*, 84(3), 245– 256. https://doi.org/10.1016/j.jenvman.2006.06.003

Moody, J. A., & Martin, D. A. (2001). Post-fire, rainfall intensity–peak discharge relations for three mountainous watersheds in the western USA. *Hydrological Processes*, 15(15), 2981– 2993. https://doi.org/10.1002/hyp.386

Moody, J. A., Shakesby, R. A., Robichaud, P. R., Cannon, S. H., & Martin, D. A. (2013). Current research issues related to post-wildfire runoff and erosion processes. *Earth-Science Reviews*, 122, 10– 37. https://doi.org/10.1016/j.earscirev.2013.03.004

Musselman, K. N., Molotch, N. P., & Brooks, P. D. (2008). Effects of vegetation on snow accumulation and ablation in a mid-latitude sub-alpine forest.

Hydrological Processes, 22(15), 2767– 2776. https://doi.org/10.1002/hyp.7050

National Operational Hydrologic Remote Sensing Center. (2004). Snow Data Assimilation System (SNODAS) Data Products at NSIDC. https://doi.org/10.7265/N5TB14TC

Nolan, R. H., Lane, P. N. J., Benyon, R. G., Bradstock, R. A., & Mitchell, P. J. (2014). Changes in evapotranspiration following wildfire in resprouting eucalypt forests. *Ecohydrology*, 7(5), 1363– 1377. https://doi.org/10.1002/eco.1463

Pierson, F. B., Robichaud, P. R., & Spaeth, K. E. (2001). Spatial and temporal effects of wildfire on the hydrology of a steep rangeland watershed. *Hydrological Processes*, 15(15), 2905– 2916. https://doi.org/10.1002/hyp.381

Richards, L. A. (1931). Capillary conduction of liquids through porous medium. *Journal of Applied Physics*, 1(5), 318– 333. https://doi.org/10.1063/1.1745010

Robichaud, P. R. (2000). Fire effects on infiltration rates after prescribed fire in Northern Rocky Mountain forests, USA. *Journal of Hydrology*, 231–232, 220– 229. https://doi.org/10.1016/S0022-1694(00)00196-7

Roche, J. W., Goulden, M. L., & Bales, R. C. (2018). Estimating evapotranspiration change due to forest treatment and fire at the basin scale in the Sierra Nevada, California. *Ecohydrology*, 11(7), e1978. https://doi.org/10.1002/eco.1978

Rulli, M. C., & Rosso, R. (2007). Hydrologic response of upland catchments to wildfires. *Advances in Water Resources*, 30(10), 2072– 2086. https://doi.org/10.1016/j.advwatres.2006.10.012

Seager, R., Ting, M., Held, I., Kushnir, Y., Lu, J., Vecchi, G., … Naik, N. (2007). Model projections of an imminent transition to a more arid climate in Southwestern North America. *Science*, 316(5828), 1181– 1184. https://doi.org/10.1126/science.1139601

Seibert, J., McDonnell, J. J., & Woodsmith, R. D. (2010). Effects of wildfire on catchment runoff response: A modeling approach to detect changes in snow-dominated forested catchments. *Hydrology Research*, 41(5), 378– 390.

Siirila-Woodburn, E. R., Steefel, C. I., Williams, K. H., & Birkholzer, J. T. (2018). Predicting the impact of land management decisions on overland flow generation: Implications for cesium migration in forested Fukushima watersheds. *Advances in Water Resources*, 113, 42– 54. https://doi.org/10.1016/j.advwatres.2018.01.008

SMAP. (2015). Soil Moisture Active Passive. Retrieved October 18, 2018, from SMAP website: https://smap.jpl.nasa.gov/

The Nature Conservancy. (2019). The nature conservancy. Retrieved January 28, 2019, from The Nature Conservancy website: https://www.nature.org/en-us/404/

USGS. (2018). USGS.gov|Science for a changing world. Retrieved October 18, 2018, from https://www.usgs.gov/

Vadilonga, T., Úbeda, X., Germann, P. F., & Lorca, M. (2008). Effects of prescribed burnings on soil hydrological parameters. *Hydrological Processes*, 22(21), 4249– 4256. https://doi.org/10.1002/hyp.7032

van Genuchten, M. T. (1980). A closed-form equation for predicting the hydraulic conductivity of unsaturated soils 1. *Soil Science Society of America Journal*, 44(5), 892. https://doi.org/10.2136/sssaj1980.03615995004400050002x

Varhola, A., Coops, N. C., Weiler, M., & Moore, R. D. (2010). Forest canopy effects on snow accumulation and ablation: An integrative review of empirical results. *Journal of Hydrology*, 392, 219– 233. https://doi.org/10.1016/j.jhydrol.2010.08.009

Welch, L. A., & Allen, D. M. (2014). Hydraulic conductivity characteristics in mountains and implications for conceptualizing bedrock groundwater flow. *Hydrogeology Journal*, 22(5), 1003– 1026. https://doi.org/10.1007/s10040-014-1121-5

Westerling, A. L., Hidalgo, H. G., Cayan, D. R., & Swetnam, T. W. (2006). Warming and earlier spring increase western U.S. forest wildfire activity. *Science*, 313(5789), 940– 943. https://doi.org/10.1126/science.1128834

Whitlock, C. (2004). Land management: Forests, fires and climate. *Nature*, 432(7013), 28– 29. https://doi.org/10.1038/432028a

Winkler, R., Boon, S., Zimonick, B., & Spittlehouse, D. (2014). Snow accumulation and ablation response to changes in forest structure and snow surface albedo after attack by mountain pine beetle. *Hydrological Processes*, 28(2), 197– 209. https://doi.org/10.1002/hyp.9574

Zhou, G., Wei, X., Chen, X., Zhou, P., Liu, X., Xiao, Y., … Su, Y. (2015). Global pattern for the effect of climate and land cover on water yield. *Nature Communications*, 6, 5918. https://doi.org/10.1038/ncomms6918

Zhou, Y., Zhang, Y., Vaze, J., Lane, P., & Xu, S. (2013). Impact of bushfire and climate variability on streamflow from forested catchments in southeast Australia. *Hydrology and Earth System Sciences Discussions*, 10(4), 4397– 4437. https://doi.org/10.5194/hessd-10-4397-2013